Atomistics informed continuum strain field of dislocations

Gorkem Gengor,[1] Orcun Koray Celebi,[1,2] Sena Pekol,[1] Daegun You,[1]
Ahmed Sameer Khan Mohammed,[1] and Huseyin Sehitoglu[1,*]
[1]*Department of Mechanical Science and Engineering, University of Illinois at Urbana-Champaign, 1206 W. Green St., Urbana, Illinois 61801, USA*
[2]*Department of Mechanical Engineering, Bilkent University, Ankara 06800, Turkey*

(Received 5 February 2025; revised 17 June 2025; accepted 20 August 2025; published 4 September 2025)

We formulate a novel methodology called the regularized Green's function method for dislocations (RGFMD) for determining the continuum elastic fields of a dislocation at the lattice scales. RGFMD utilizes the quantum mechanical force density (QMFD) to represent atoms within the elastic media without creating any singularities in the elastic fields. QMFD is related to the electron wave functions, which is a fundamental result of density functional theory (DFT) calculations. RGFMD solves the force equilibrium equation where QMFD is used to represent atomic displacements via computationally efficient Fourier transforms. The quasiperiodic nature of dislocations is accounted for by introducing the periodic images of individual atoms along the dislocation line. The advantage of RGFMD over existing classical elasticity solutions and atomistic simulations for dislocations is threefold. First, RGFMD guarantees the production of well-behaving bounded elastic fields, whereas classical elasticity frameworks diverge at the dislocation core. Second, classical elasticity frameworks are built upon the assumption of plane strain conditions, which limits their ability to realistically capture variations in the elastic fields along the dislocation line. RGFMD accurately accounts for the local atomic configuration and does not imply simplifying conditions such as plane strain. Third, atomistic calculations can report elastic quantities such as displacements only at the lattice sites, which precludes their full integration with well-established continuum field theories. RGFMD bridges this gap between atomistic and continuum theories by mapping out continuum elastic fields using the discrete displacement data provided by DFT calculations.

DOI: 10.1103/nspp-zy5m

I. INTRODUCTION

Dislocations have been shown to affect numerous material properties that are vital for engineering applications. Such material properties include, but are not limited to, material strength [1–11], ductility [12], fatigue resistance [13–17], electrical conductivity [18–21], diffusivity [22], hydrogen embrittlement resistance [23,24], and quantum spin coherence [25]. These properties play a crucial role in applications ranging from structural applications to quantum computing and information. Past research has shown that these properties are affected by the elastic interactions between dislocations and other dislocations [5,26–28], point defects [29–31], and interfaces [32–35] in crystals. Traditionally, there have been two approaches to investigate the dislocations' elastic fields and interactions.

Dislocations are modeled as continuum elastic fields through anisotropic elasticity solutions. The state-of-the-art solutions for dislocation elastic fields are given by the Eshelby-Stroh (ES) formulation [36–38]. Even though ES formulation provides accurate information about the dislocation's displacement field in the long-range regime, it diverges at the core of the dislocation due to the assumption of applied point load at the dislocation line. It has been conventional to disregard the effect of the core's elastic field in elasticity calculations [39]. Moreover, the plane strain assumption implies that any variations in elastic fields along the dislocation line are disregarded [see Fig. 1(a)]. Hence, obtaining a full picture of elastic characteristics of dislocations requires one to accurately model the elastic fields within the core. The Peierls-Nabarro (PN) model for dislocations is proposed to mathematically remove the singularity at the dislocation cores. The PN model models dislocations as a distribution of infinitesimal dislocations with Burgers vectors summing up to the total Burgers vector of the full dislocation. Even though PN predicts bounded elastic fields, it still implicitly assumes plane strain conditions and does not account for the local atomic displacements near the core [see Fig. 1(b)].

Dislocation core structures are simulated via atomistics and density functional theory (DFT) calculations. These techniques can provide valuable information about the atomic configuration in the vicinity of the dislocation cores, which is missing in continuum elasticity solutions. A major drawback for the atomistics is that it is not possible to decouple the elastic interactions from boundary conditions such as periodic boundaries and free surfaces [39–41]. Moreover, atomistic methods model every atom as point-like entities located at nuclei positions, and information such as energy, force, or displacements are only attributed to these nuclei positions. Therefore, care is necessary when utilizing atomistic calculations to construct continuum descriptions [42] since obtaining the strain solutions by averaging the relative displacements of neighboring atoms within a predefined cutoff radius is not

*Contact author: huseyin@illinois.edu

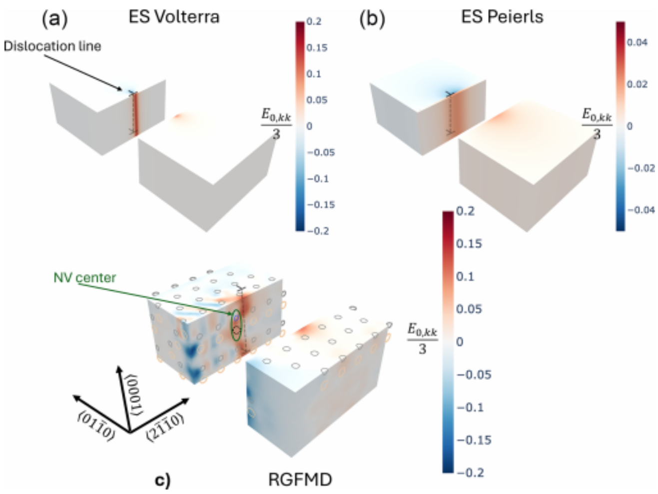

FIG. 1. Logarithmic dilatational strain field of a TED core in 4H-SiC as calculated by classical models, and RGFMD. (a) Strain field of a Volterra dislocation is calculated for anisotropic elasticity constants of 4H-SiC using ES formalism. Note the singularity at the core created by the Volterra dislocation. (b) Dilatational strain field of a PN dislocation is calculated by utilizing ES formalism. (c) Dilatational strain field is calculated using RGFMD, a novel framework suggested in this study. See text for the details.

reliable for capturing an accurate field. The former is given as discrete data located at lattice sites, while the latter is a field description. Further comparisons of the strain fields associated with the above approaches are given in Appendix D.

An encompassing theory for dislocations should address the following two challenges: it should be nonsingular at the core and it should be able to account for the local atomic configuration at the core where the Cauchy-Born hypothesis may not hold. The Cauchy-Born hypothesis states that the displacements of atoms within the crystal follow the overall strain on the crystal [43,44]. This study focuses on developing a scheme that uses the results of DFT calculations, such as electron wave functions and electron densities, to give a continuum description of dislocation cores. Recently, we proposed the regularized Green's function method (RGFM) to utilize electron wave functions and band structure to determine nonsingular continuum elastic fields for point defects [42]. This was accomplished by introducing nonsingular Green's functions, which are a product of quantum mechanical force fields representing atoms within the crystal. RGFM relates these force fields to the atomistic displacements to capture the atomic configuration of the lattice in the vicinity of the defect core. In this study, we extend RGFM to account for the periodicity of dislocations along the dislocation lines and name it the regularized Green's function method for dislocations (RGFMD). RGFMD addresses all the challenges mentioned above by representing individual atoms via their quantum mechanical force densities and accounting for the local atomic displacements near core region. The details of the RGFMD framework are discussed in Sec. II A. RGFMD can accurately predict elastic fields of dislocations without any assumption of plane strain conditions or unphysical singularities even in the presence of point defects [see Fig. 1(c)] in the presence of a nitrogen-vacancy (NV center in SiC). RGFMD also unveils the variations of elastic fields along the dislocation line which was missed in classical elasticity solutions. Also, we would like to point out that RGFMD is not devised to be a stand-alone tool for simulating dislocations. Our aim with the RGFMD is to extract maximal information from a single DFT simulation of a dislocation. In fact, RGFMD provides a unique perspective on the morphology of dislocation cores by relating the electronic structure of the core with the micromechanics of the dislocation.

In our demonstration of extended RGFM, we chose threading edge dislocations in 4H-SiC crystals as a model case. 4H-SiC has been shown to be a promising candidate for quantum computing applications due to the superior quantum spin properties of NV centers within its host lattice [45–49]. The spin coherence time of NV centers is sensitive to the lattice distortions around them [50], creating the possibility of tuning the spin coherence time via utilizing dislocations within 4H-SiC crystals. In the following section, we give an overview of the different slip systems that are found in bulk and wafer samples of 4H-SiC.

Slip systems in 4H-SiC

Bulk and wafer 4H-SiC samples contain a variety of dislocations. Figures 2(a)–2(c) illustrate the geometry of different common dislocation configurations. Fundamental lattice vectors are shown as an inset in Fig. 2(a). Dislocations in 4H-SiC are divided into two main categories depending on where their dislocation line ξ lies in: Basal plane dislocations (BPDs) as ξ lie in the basal plane [see Fig. 2(a)] and threading dislocations (TDs) as ξ lie along c axis [see Figs. 2(b) and 2(c)]. Solid lines mark the dislocation lines within the substrate and the epilayer. The orientations of the primitive unit cell are shown in the insets. We elaborate on this complexity in the details below.

BPDs have the Burgers vector of $\frac{1}{3}\langle 2\bar{1}\bar{1}0\rangle$ which lies in the basal plane. In bulk samples, BPDs are found to dissociate into two partials with Burgers vectors $\frac{1}{3}\langle 10\bar{1}0\rangle$ and $\frac{1}{3}\langle 01\bar{1}0\rangle$. These partials form a stacking fault in between where the pristine stacking of the crystal is altered. The width of the stacking faults was observed to be between 40–50 nm. The length scale of the stacking faults (in the order of nm) precludes the direct simulation of BPD cores within the DFT framework due to computational power and memory limitations. Moreover, BPDs and the stacking faults that form when they dissociate have been shown to degrade the electrical properties of the 4H-SiC electronic devices [18–21]. Hence, a considerable effort has been dedicated to the development of manufacturing techniques that would prevent them from forming within epitaxial layers (wafer samples). The state-of-the-art production technique for 4H-SiC is step controlled chemical vapor deposition (CVD), where an epitaxial layer is deposited onto a single crystal substrate of 4H-SiC (bulk sample). The reader is referred to [51,52] for a detailed discussion of this technique. During the CVD process, over 95% of the BPDs in the bulk substrate are transmitted into the epitaxial layer as threading edge dislocation (TED) [53,54]. See Fig. 2(d) for transmission rates of different dislocations in the bulk substrate into the epitaxial layer. Due to the low transmission rate of BPDs,

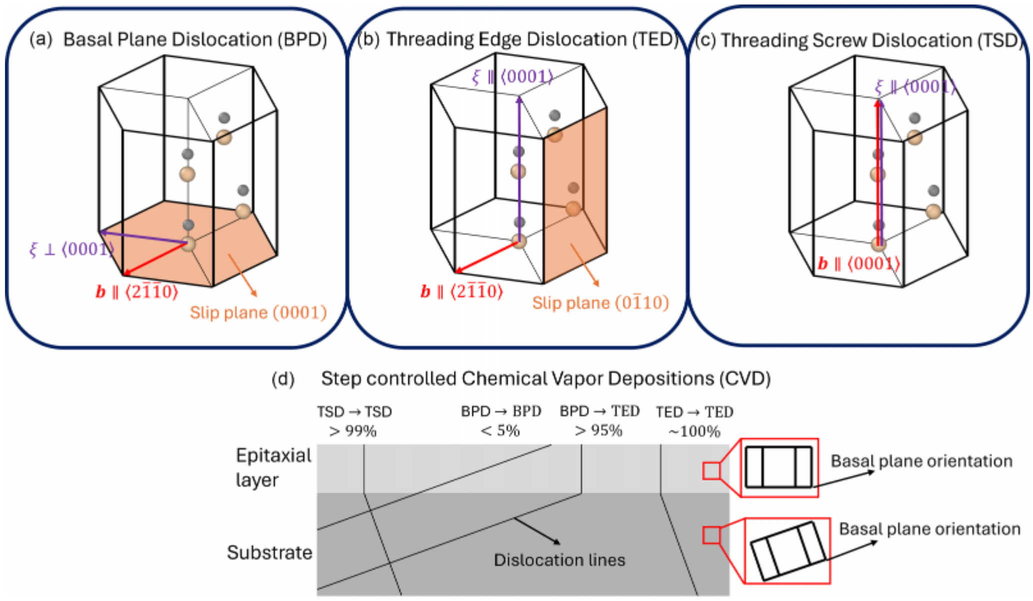

FIG. 2. The three prominent slip systems in 4H-SiC. (a) An edge character BPD is illustrated. These dislocations, which have Burgers vector along the $\langle 2\bar{1}\bar{1}0\rangle$ axis and dislocation line within the basal plane, are prevalent in bulk samples of 4H-SiC. (b) TEDs are the most prominent dislocations in wafer samples of 4H-SiC. TEDs have their Burgers vector along $\langle 2\bar{1}\bar{1}0\rangle$ but their dislocation line lies along the $\langle 0001\rangle$ axis. (c) TSDs have Burgers vector and dislocation line along the $\langle 0001\rangle$ axis. (d) During CVD, an epilayer of 4H-SiC is deposited onto a 4H-SiC crystal. The existing dislocations in the bulk layer (dark grey region) are converted into dislocations in the epilayer (light gray region). Solid lines mark the dislocation lines.

the properties of 4H-SiC devices are dictated by TEDs and threading screw dislocations (TSDs).

The density of different types of dislocations in substrate and epitaxial layers are summarized in Table I. TSDs have a Burgers vector and dislocation line along the c axis, $\langle 0001\rangle$, and are recognized to have undesirable effects on the reliability of electrical devices [53–55]. TSDs cause large atomic displacements at the core, as the length of the c axis is nearly three times the a vector for 4H-SiC. TEDs have Burgers vector equal to $a = \frac{1}{3}\langle 2\bar{1}\bar{1}0\rangle$ and the dislocation line along the c axis, $\langle 0001\rangle$. TEDs have the highest density among the dislocations in commercial 4H-SiC devices. Their relatively small Burgers vector makes it more convenient for DFT calculations properties. It is imperative to improve our understanding of the elastic effects of TEDs on the host lattice to better leverage 4H-SiC in electrical and quantum computing devices. Therefore, by choosing TEDs as a model case, we hope to provide valuable insight into the underlying physics of TEDs.

II. METHODS AND RESULTS

The ES formalism offers a general solution framework for anisotropic elasticity problems, assuming that the elastic field is two-dimensional, i.e., elastic fields do not vary along the dislocation line. Even though ES formalism produces accurate results for elastic fields at long ranges, it produces divergent fields near the dislocation core. Therefore, conventional studies define a dislocation core region and exclude this region from the calculations [39]. Commonly, this core region is selected as a circular region of radius $\sim 5b$ where b is the magnitude of the Burgers vector of the dislocation. Recently, the authors proposed a RGFM for point defects. Moreover, RGFM removes (regularizes) singularities that are present in the elastic Green's function by representing atoms within the lattice as a distribution of distributed loads. These representative force densities are a product of the electron wave functions of the given crystals.

In Sec. II A, we extend our RGFM formulation to account for the quasiperiodic nature of the dislocations. Dislocations are quasiperiodic because their elastic fields must be periodic along the dislocation line with a periodicity equal to the periodic lattice spacing in that crystallographic direction. This periodicity has been completely omitted in the conventional continuum treatment of dislocations. Also, electron wave functions can be determined via *ab initio*. calculations, as discussed in Sec II B. We envision our novel treatment of dislocation cores to bridge the gap between the continuum and atomistic treatment of dislocations. In Sec. II C, we apply our model to a TED in the 4H-SiC host lattice. These dislocations are shown to be the most pervasive in wafers [53,54] and affect the mechanical properties and electronic reliability of SiC electronic devices. Moreover, 4H-SiC can host NV centers which are promising spin defects for quantum computing applications due to their superior coherence times [45,50]. Both experimental and theoretical studies have shown that the coherence times of NV centers are sensitive to

TABLE I. Densities of dislocations in 4H-SiC.

Dislocation type	Density in bulk (cm^2)	Density in epilayer (cm^2)
BPD	10^2–10^4	0.1 − 10
TED	10^3–10^4	2000–5000
TSD	10^2–10^3	300–1000

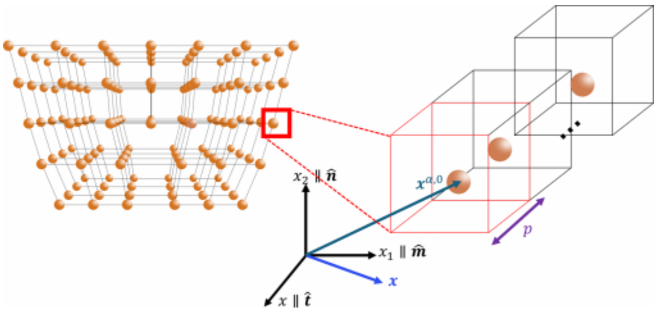

FIG. 3. Atomic structure of a dislocation in the lattice. Dislocations are quasiperiodic since they create displacement fields that are varying in three dimensions, but their displacement field is periodic along their dislocation line. As a result, an atom within the dislocated crystal has infinitely many periodic images along the dislocation line. The periodic distance between an atom and its nearest images $\boldsymbol{p}$ is determined by the lattice periodicity along the dislocation line. RGFMD accounts for this periodicity by defining the atomic force profile representing an atom as a quasiperiodic function. See text for details.

applied strain. The spin-strain coupling of NV centers raises the question of whether dislocations within 4H-SiC can be used to tune the properties of NV centers. Hence, we envision RGFMD to provide valuable insight into understanding the elastic interactions between NV centers and lattice defects.

A. Development of regularized Green's function method for dislocations

The RGFM is devised to solve the force equilibrium equation in three dimensions for point defects. Within RGFM, the atomic displacements induced by a point defect are calculated via DFT calculations and used as boundary conditions for continuum displacement field calculations. RGFM models every atom that is simulated in the DFT simulation box as distributed force density, called the quantum mechanical force density (QMFD) field. The QMFD field can be calculated from the first-principles quantities such as electron wave functions and densities. Point defects within crystal lattices do not create any geometrical periodicity. Hence, RGFM models the elastic distortions caused by point defects by solving the force equilibrium for infinite media. However, in lattice length scales, dislocation-induced elastic fields must obey the inherent periodicity of the underlying lattice. For a straight dislocation, while the atomic arrangement around the dislocation varies along the dislocation line within *one unit-cell*, atomic displacements must be periodic from one unit-cell to its periodic image (see Fig. 3). Therefore, the displacement field of a dislocation must be a *quasiperiodic* function of the position with respect to the dislocation line with a periodicity that is dictated by the periodic lattice spacing along the dislocation line. A quasiperiodic function is a function that is periodic with respect to a subset of its inputs [56]. In this section, we derive RGFM formalism following [42] and extend it to account for the quasiperiodic nature of the dislocations.

RGFMD aims to solve the force equilibrium equation of elasticity for dislocations in a manner that is informed by *ab initio* calculations. Force equilibrium equation is satisfied nearly universally across different domains such as solid, fluid, and quantum regimes [57–60].

$$C_{ijkl}\frac{\partial^2 G_{kn}(\boldsymbol{x})}{\partial x_j \partial x_l} + \delta_{in} f(\boldsymbol{x}) = 0, \tag{1}$$

where $f(\boldsymbol{x})$ is the forcing function, $\boldsymbol{G}(\boldsymbol{x})$ is the Green's function, $\boldsymbol{C}$ is the anisotropic elasticity tensor, and δ_{in} is the Kronecker delta. In conventional methods, the forcing function is assumed to be a point force represented by a Dirac delta function $\delta(\boldsymbol{x})$. We regularize the Green's function by choosing the forcing function $f(\boldsymbol{x})$ as the QMFD field representing the individual atoms in the system instead of a point load. The calculation of QMFD is discussed later in this section.

The solutions to Eq. (1) can be obtained by taking the Fourier transform

$$\hat{G}_k \;\; = (C_{ijkl}\xi_j\xi_l)^{-1}\delta_i \;\; \hat{f}(\boldsymbol{\xi}), \tag{2}$$

where the hat symbol $\hat{y}$ represents the Fourier transform of a variable y and $\boldsymbol{\xi}$ is the wave vector. The real-space solution to Eq. (1) can be found by taking the inverse Fourier transform of Eq. (2)

$$\boldsymbol{G}(\boldsymbol{x}) = \frac{1}{8\pi^3}\iiint_{-} \;\; \hat{\boldsymbol{G}}(\boldsymbol{\xi})e^{i\boldsymbol{x}\cdot\boldsymbol{\xi}}d\boldsymbol{\xi}. \tag{3}$$

However, direct calculation of the inverse Fourier integral in three dimensions is computationally costly. Hence, we employ the spherical harmonic expansion of plane waves $e^{i\boldsymbol{x}\cdot\boldsymbol{\xi}}$ [61]

$$e^{i\boldsymbol{k}\cdot\boldsymbol{x}} = 4\pi\sum_{n=0}\sum_{m=-n}^{n} i^l j_n(|\boldsymbol{x}||\boldsymbol{k}|)Y_n^m(\tilde{\boldsymbol{x}})Y_n^m(\tilde{\boldsymbol{k}}), \tag{4}$$

where $Y_n^m(\tilde{\boldsymbol{k}})$ is the spherical harmonic function of degree n and order m, $\bar{Y}_n^m(\tilde{\boldsymbol{k}})$ is its complex conjugate, and $j_n(\cdot)$ is the spherical Bessel function of degree n. We also denote unit vectors as $\tilde{\boldsymbol{x}} = \boldsymbol{x}/|\boldsymbol{x}|$. The Green's function in Eq. (3) takes the following form:

$$G_k \;\; (\boldsymbol{x}) = \frac{1}{2\pi^2}\sum_{n=0}\sum_{m=-n}^{n} i^n Y_n^m(\tilde{\boldsymbol{x}})\iiint_{-} \;\; \delta_i \;\; \hat{f}(\boldsymbol{\xi})(C_{ijkl}\xi_j\xi_l)^{-1} \times j_n(|\boldsymbol{x}|\boldsymbol{\xi})\bar{Y}_n^m(\tilde{\boldsymbol{\xi}})d\boldsymbol{\xi}. \tag{5}$$

If the forcing function $f(\boldsymbol{x})$ is taken as a spherical function $f(\boldsymbol{x}) = f(|\boldsymbol{x}|)$, a further simplification to Eq. (5) is possible as follows:

$$\boldsymbol{G}(\boldsymbol{x}) = \frac{1}{2\pi^2}\sum_{n=0}\sum_{m=-n} i^n Y_n^m(\tilde{\boldsymbol{x}})\int_0 \;\; \hat{f}(|\boldsymbol{x}|)j_n(|\boldsymbol{x}||\boldsymbol{\xi}|)d|\boldsymbol{\xi}| \times \int_{S^2}\left(C_{ijkl}\tilde{\xi}_j\tilde{\xi}_l\right)^{-1}\bar{Y}_n^m(\tilde{\boldsymbol{\xi}})dS(\tilde{\boldsymbol{\xi}}),$$

$$\boldsymbol{G}(\boldsymbol{x}) = \frac{1}{2\pi^2}\sum_{n=0}\sum_{m=-n}^{n} i^n Y_n^m(\tilde{\boldsymbol{x}})F_n(|\boldsymbol{x}|)\cdot\boldsymbol{A}_n^m(\boldsymbol{C}). \tag{6}$$

Equation (6) is composed of two main parts: radial $F_n(|\boldsymbol{x}|)$, and angular $\boldsymbol{A}_n^m(\boldsymbol{C})$ part. The radial part is a function of the forcing function $f(\boldsymbol{x})$ and the distance between the nuclei position and the field point. $F_n(|\boldsymbol{x}|)$ can be computed beforehand

and interpolated at a run-time with arbitrary precision. $\boldsymbol{A}_n^m(\boldsymbol{C})$ only depends on the anisotropic elasticity tensor $\boldsymbol{C}$ and can be computed beforehand for fast implementation. It is also shown that the terms in the sum above is nonzero only when n is an even integer which reduces the computational cost [42,62]. Moreover, the infinite sum can be truncated at a certain value of $n = n_{\max}$. For 4H-SiC anisotropy, we showed in our previous study that $n_{\max} = 8$ produces accurate convergence for our purposes [42].

The solution given in Eq. (6) implicitly assumes an infinite solid body with no periodic boundaries. However, the dislocations' displacement field must be periodic along their dislocation line with a periodic equal to the lattice spacing along the dislocation line. This periodicity requires us to consider every atom within the simulation cell and its periodic images. Let the dislocation line lie along a crystallographic direction $\hat{\boldsymbol{t}}$, the periodic lattice spacing along $\hat{\boldsymbol{t}}$ to be p, and the position of an arbitrary atom (with index number α) within the simulation cell to be $\boldsymbol{x}^\alpha$. Then, the position of every periodic image of the atom α can be computed as follows:

$$\boldsymbol{x}^{\alpha,k} = \boldsymbol{x}^\alpha + kp\hat{\boldsymbol{t}}, \qquad k \in \mathbb{Z} \tag{7}$$

The RGFM represents the elastic deformation at point $\boldsymbol{x}$ due to the displacement of an atom at $\boldsymbol{x}^\alpha$ by the Green's function $\boldsymbol{G}^\alpha(\boldsymbol{x} - \boldsymbol{x}^\alpha)$. Using Eq. (7), the total Green's function representing the elastic deformation at the field point $\boldsymbol{x}$ due to the atom at $\boldsymbol{x}^\alpha$ and its periodic images takes the following form:

$$\boldsymbol{G}^D(\boldsymbol{x}) = \sum_{k=0} \boldsymbol{G}(\boldsymbol{x} - \boldsymbol{x}^\alpha - kp\hat{\boldsymbol{t}}) + \boldsymbol{G}\big(\boldsymbol{x} - \boldsymbol{x}^\alpha + kp\hat{\boldsymbol{t}}\big), \quad k \in \mathbb{Z}^+ \tag{8}$$

For practical implementations of Eq. (8), the infinite sum must be truncated. The truncation limit depends on the specific system under consideration. See Appendix A for the details regarding the determination of the truncation limit for the case of 4H-SiC. So far, we extended our RGFM formalism into dislocations. In the next section, we calculate the QMFD to inform our choice of forcing function $f(|\boldsymbol{x}|)$ in RGFMD formalism.

Using RGFMD, the elastic displacement at any point due to the displacement of the atoms forming the configuration under consideration can be calculated as follows:

$$\boldsymbol{u}(\boldsymbol{x}) = \sum_{\alpha=1}^{N} \boldsymbol{G}^{D,\alpha}(\boldsymbol{x} - \boldsymbol{x}^\alpha) \cdot \boldsymbol{h}^\alpha \tag{9}$$

where parameter $\alpha = 1, 2, \dots, N$ enumerates the atoms in the system, $\boldsymbol{x}^\alpha$ is the position of atom α, and $\boldsymbol{G}^{D,\alpha}$ is the quasiperiodic Green's function that represents atom α and its images in the system with dislocation. The vectors $\boldsymbol{h}^\alpha$ are scaling vectors that are calculated for each atom using the known atomic displacements. The displacement of atom β is equal to the sum of elastic distortion caused by every individual atom in the system.

$$\boldsymbol{u}^\beta(\boldsymbol{x}^\beta) = \sum_{\alpha=1}^{N} \boldsymbol{G}^{D,\alpha}(\boldsymbol{x}^\beta - \boldsymbol{x}^\alpha) \cdot \boldsymbol{h}^\alpha \tag{10}$$

Since the displacement of all the atoms can be obtained using *ab initio* simulation techniques, scaling vectors $\boldsymbol{h}^\alpha$ can be solved for by forming a $3N \times 3N$ dense linear system of equations using Eq. (10). So far, an efficient algorithm to determine the elastic fields of a dislocation core, RGFMD, has been presented. However, RGFMD requires one to determine the force fields representing the individual atoms. In Sec. II B, expressions for atomic representative force density field, QMFD, are derived.

B. Quantum mechanical rorce density

Our derivation of RGFMD, requires one to determine the forcing function $f(\boldsymbol{x})$ as a radial function to represent individual atoms within the continuum. We base our choice of the forcing function onto the first-principles calculations by calculating QMFD. QMFD is the divergence of the quantum mechanical stress density (QMSD), $\partial_j\sigma_{ij} = f_i$ [59,63–67]. Rogers and Rappe derived QMSD from purely geometric arguments by defining stress as the variation of the energy with respect to strain [66]. QMSD becomes as follows in atomic units:

$$\begin{aligned}\sigma_{ij} = \frac{\hbar^2}{m_e}\Bigg(&-\frac{\partial\psi^\dagger}{\partial r_i}\frac{\partial\psi}{\partial r_j} + \gamma\left(\frac{\partial^2 n}{\partial r_i \partial r_j} - \delta_{ij}\frac{\partial^2 n}{\partial r_k \partial r_k}\right)\\ &+ \frac{1}{4}\delta_{ij}\frac{\partial^2 n}{\partial r_k \partial r_k}\Bigg) + \delta_{ij} n\epsilon^{\mathrm{GGA}} + \frac{\partial(n\epsilon^{\mathrm{GGA}})}{\partial n}\frac{\partial n}{\partial \ \ _{ij}}\\ &+ \frac{\partial(n\epsilon^{\mathrm{GGA}})}{\partial(\nabla n)}\frac{\partial(\nabla n)}{\partial \ \ _{ij}} + \epsilon_0\left(F_iF_j - \frac{1}{2}\delta_{ij}F_kF_k\right),\end{aligned} \tag{11}$$

where ψ and $\psi^\dagger$ are the electron wave function and its complex conjugate, $n = \psi^\dagger\psi$ is the electron density, ϵ^{GGA} is the per electron exchange correlation energy density according to the generalized gradient approximation (GGA) [67], $\ _{ij}$ is the strain, ϵ_0 is the vacuum permittivity, and $F_i = -\partial_i V$ is the electric field. Contributions to QMSD can be divided into three main groups: the kinetic stress [the first line in Eq. (11)], the exchange-correlation contributions [the second line in Eq. (11)], and electrostatic contributions [the third line in Eq. (11)].

The kinetic contribution to QMSD appears due to the kinetic energy of electrons. The kinetic energy density in quantum mechanics is said to be gauge dependent [64,66,67]. The gauge dependence of the kinetic energy density is represented by the real-valued parameter γ. However, the term that is multiplied with the gauge dependence term is divergence free, $\partial_j(\frac{\partial^2 n}{\partial r_i \partial r_j} - \delta_{ij}\frac{\partial^2 n}{\partial r_k \partial r_k}) = 0$. Hence, we set $\gamma = 0$ for our calculations without loss of generality. The kinetic contribution to QMSD takes the following form:

$$f_i^K = \frac{\partial}{\partial r_j}\left(-\frac{\partial\psi^\dagger}{\partial r_i}\frac{\partial\psi}{\partial r_j} + \frac{1}{4}\frac{\partial^2 n}{\partial r_k \partial r_k}\right). \tag{12}$$

The contribution from exchange-correlation effects to QMSD $f_i^{\mathrm{GGA}} = \partial_j\sigma_{ij}^{\mathrm{GGA}}$ [second line of Eq. (11)] can be computed via numerical differentiation once the electron density field n is known. For practical applications, the values of terms $\frac{\partial(n\epsilon^{\mathrm{GGA}})}{\partial n}$ and $\frac{\partial(n\epsilon^{\mathrm{GGA}})}{\partial(\nabla n)}$ are reported by the libraries that are used to calculate exchange-correlation energy density such as libxc [68]. Finally, the third line of Eq. (11) is also known as the Maxwell stress tensor [59,66,67,69]. Its divergence is known as the Lorentz force [69] and represents the

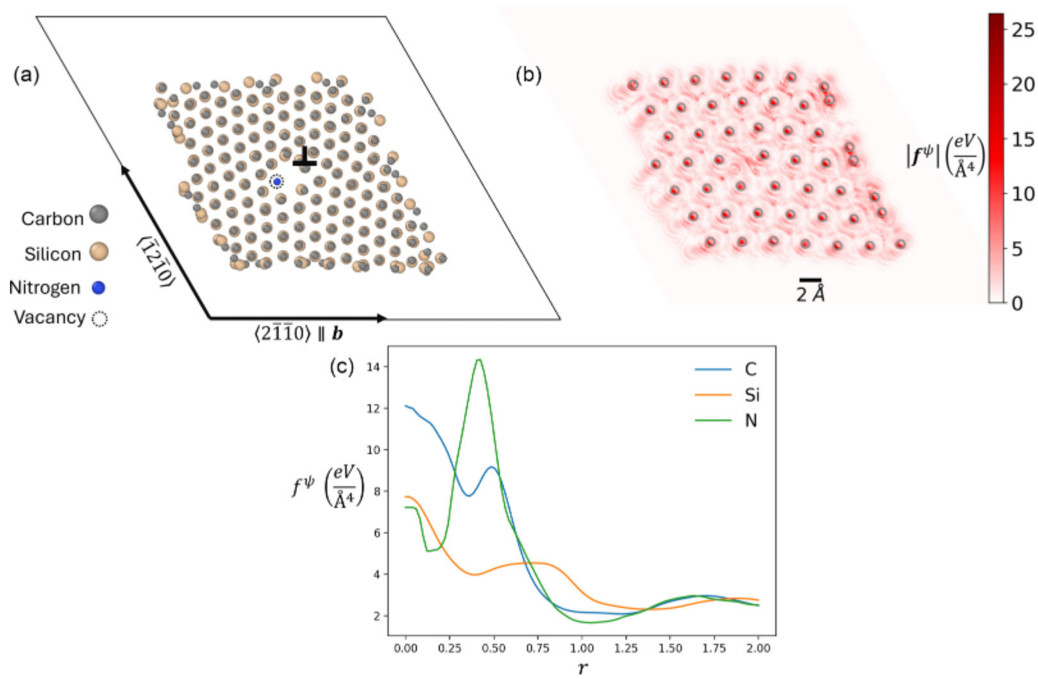

FIG. 4. (a) The relaxed structure of the crystal with NV center and a TED core. To generate an isolated TED core, a vacuum region surrounding the crystal is introduced while the periodic boundary along the dislocation line is preserved. The location of the dislocation core is marked in the figure. (b) QMFD field's projection onto basal plane is plotted. The resulting force density $\boldsymbol{f}^{\psi}$ localizes around the lattice sites. (c) Spherical average of the force profiles of the different species in the system.

electrostatic contribution to QMFD.

$$f_i^{ES} = \frac{\partial}{\partial r_j}\left[\epsilon_0\left(F_iF_j - \frac{1}{2}\delta_{ij}F_kF_k\right)\right] = -n\frac{\partial V}{\partial r_i}, \qquad (13)$$

where V is the electrostatic potential. QMFD is defined by a vector valued function. To use the spherical harmonic decomposition given in Sec. II A, we take the magnitude of QMFD everywhere and average it on the spherical shells around the atomic sites as follows:

$$f^{\psi}(|\boldsymbol{x}|) = \frac{1}{4\pi|\boldsymbol{x}|^2}\int_0^{2\pi}\int_0^{\pi}|\boldsymbol{f}^K(\boldsymbol{x}) + \boldsymbol{f}^{\text{GGA}}(\boldsymbol{x}) + \boldsymbol{f}^{ES}(\boldsymbol{x})||x|^2\sin\theta\, d\theta\, d\varphi \qquad (14)$$

These average functions $f^{\psi}(|\boldsymbol{x}|)$ are employed to represent different atomic species (such as Si, C, N) within RGFMD formalism.

In the current study, we chose TEDs in 4H-SiC crystal as a model case. To show the robustness of RGFMD formalism in studying the interactions between point and line defects, as an added complication to our study, we placed an NV point defect near the dislocation core. The results of QMFD calculation for TED-NV system are given in Fig. 4 as an example. The details of the DFT calculation are discussed in Sec. II C. It can be seen in Fig. 4(b) that the force densities localize around the atomic sites. This localization is important because it enables RGFMD to describe elastic distortions as the linear combination of Green's f.unctions. Furthermore, the magnitude QMFD exhibits a strong dependence on radial distance from the atomic sites. The RGFMD framework exploits this dependence by modeling the atomic force profiles as radial functions to solve force equilibrium equation in an efficient manner as discussed in Sec II A. Finally, the radial force profiles f^{ψ} representing individual species are nontrivial nonconstant functions as shown in Fig. 4(c). The QMFD operator is spherically averaged around the lattice sites to generate radial force density functions representing individual atoms. Different species generate different force profiles which are used to represent them in the RGFMD framework as discussed in Sec. II A.

Note that Fig. 4(c) gives the force profiles for atoms in the relaxed configuration of the TED system while Eq. (10) refers to perfect lattice positions with indices α and β. However, upon comparison between Fig. 4(c) and force profiles for the nondislocation 4H-SiC structure given in [42], we observe that the introduction of TED causes a negligible variation in Si and C profiles. Hence, the use of force profiles derived from a relaxed structure is appropriate in our context. Conventional methods based on Eshelby's equivalent inclusion method expects these properties to be constant [70,71]. It is imperative to utilize QMFD to accurately calculate lattice distortions around lattice defects.

C. Simulation details

A considerable body of research effort has been devoted to the simulation of screw dislocations within the DFT setting [72–77]. Simulating dislocations within DFT poses one major challenge. The DFT framework necessitates the simulation cell to be periodic in all three directions. Therefore, previous studies focused on simulating dipoles of dislocations with opposing Burgers vectors since the net zero sum of Burgers vector content in the simulation box permits the periodicity to be achieved. To examine an isolated dislocation core via

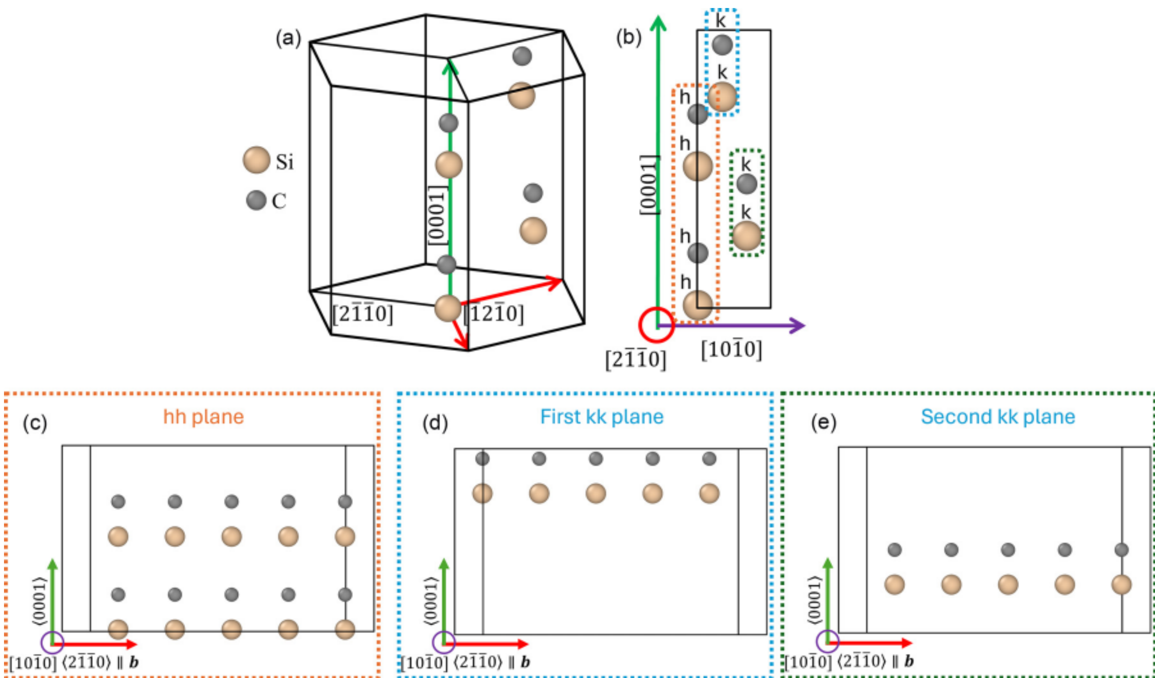

FIG. 5. (a) The atomic positions within 4H-SiC crystal. (b) 4H-SiC primitive unit cell is shown through $\langle 2\bar{1}\bar{1}0\rangle$ (the Burgers vector of TED). Atomic sites within 4H-SiC have different local symmetries and labeled as *h* and *k* sites. One can identify three slip planes normal to the $\langle 10\bar{1}0\rangle$ direction for TED slip system within 4H-SiC primitive cell. Two of these planes consist of *k* sites and named *kk* planes, while one of them consists of *h* sites and named the *hh* plane. Hence, two different types of TED cores may exist between the *hh* and *kk* planes, and two *kk* planes. (c)–(e) Projection of *hh* and *kk* planes through the slip plane normal $\langle 10\bar{1}0\rangle$. *hh* and *kk* planes have different atomic densities.

RGFMD, we simulate a block of crystal that is periodic along the dislocation line and surrounded by vacuum on the other two directions. We note that the high lattice resistance of 4H-SiC (in the GPa range [78,79]) hinders the dislocation migration toward the free surface. A TED with Burgers vector $\langle a\rangle = 1/3\langle 2\bar{1}\bar{1}0\rangle$ and dislocation line $\langle c\rangle = \langle 0001\rangle$ is studied. TED is chosen as the model case for RGFMD since TEDs are the most prevalent dislocations within 4H-SiC wafers and are more likely to affect quantum and electrical properties [20,45,50] as discussed in Sec. I A.

To accurately construct the dislocation core of a TED, we first examine the structure of its slip plane $(1\bar{1}00)$. The 4H-SiC lattice is a multilattice where the primitive unit cell contains more than one lattice site [there are eight lattice sites in this case, see Fig. 5(a)] as opposed to single-lattices which can be constructed by just repeating one lattice site along lattice vectors. The lattice sites within 4H-SiC have different local symmetries and are denominated as the *h* site or *k* site as shown in Fig. 5(b) [45]. These lattice sites form three distinct $(1\bar{1}00)$ slip planes of which two are formed by *k* sites (*kk* planes) and one is formed by *h* sites (*hh* planes). When viewed through the slip plane normal $\langle 10\bar{1}0\rangle$, the *hh* plane and *kk* planes have different atomic densities [see Figs. 5(c)–5(e)]. Hence, *kk* planes are equivalent to each other while the *hh* plane is dissimilar. This situation raises the question over which slip configuration is energetically more favorable: the slip between *hh* and *kk* planes or the slip between two *kk* planes. Such questions do not occur in single lattices such as face-centered cubic (FCC) and body-centered cubic (BCC) ones. When we consider other multilattice hexagonal close packed (HCP) crystals, the prevalent slip systems operate by displacing planes of the same atomic densities on top of each other [11]. Hence, we chose to place the dislocation core between two *kk* planes in our simulations. However, further research is warranted to clarify the atomic motions during slip in multilattices such as 4H-SiC. Even though this is an interesting future research direction, it is out of the current study's scope.

To analyze the elastic interactions between dislocations and point defects, we inserted an NV center in the vicinity of the TED core. NV centers are point defects within 4H-SiC host crystals that are formed by substituting a C atom with an N and vacating a Si site next to it. Four different configurations of NV centers are observed within 4H-SiC: *hh*, *kk*, *hk*, and *kh* [see Fig. 5(b)]. These configurations are identified via their local point symmetry groups. Among the four, *hh* and *kk* configurations are shown to be the most promising for quantum computing applications [45]. Without loss of generality, we chose to insert a NV center in the *hh* configuration near the TED core for our demonstration purposes.

The DFT simulations are conducted by using the Vienna *Ab initio* Simulation Package (vasp) [80]. Projector augmented wave (PAW) pseudopotentials as supplied with the vasp package are used in the calculations [81,82]. The exchange-correlation effects are modeled with the Perdew-Burke-Ernzerhof (PBE) parametrization of the GGA [83]. Convergence is assumed to be achieved when the total energy of the system is reached within 0.5 meV. The *ab initio* calculation of the TED-NV system is carried out as follows.

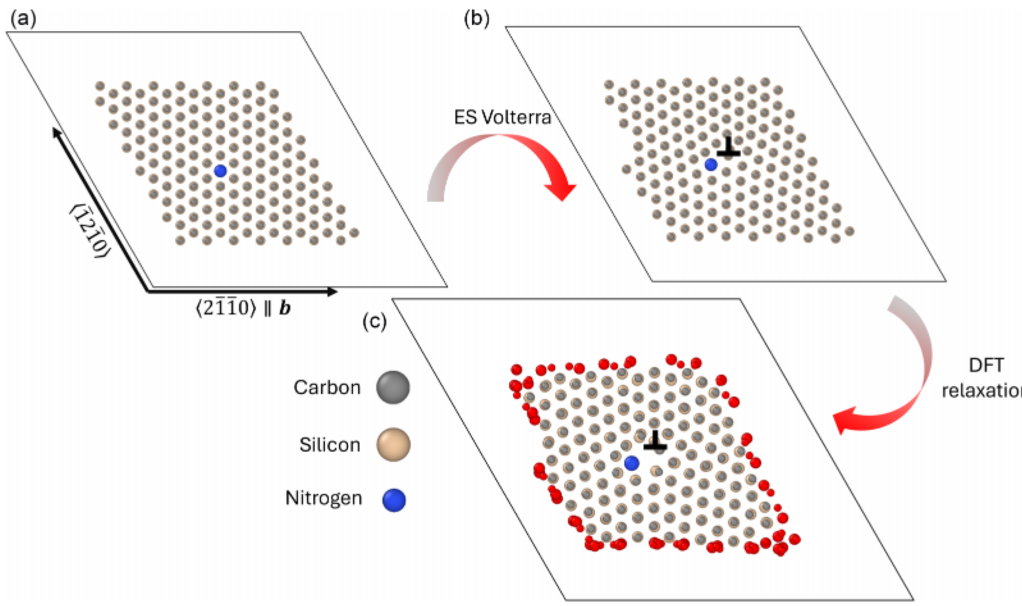

FIG. 6. The procedure that is devised to simulate an isolated TED and a NV center in a fully periodic cell in DFT framework. (a) A pristine crystal of 4H-SiC is created with 392 atoms. Subsequently, an NV center in *hh* configuration near the center of the box is inserted by replacing one C atom (marked in gray) with N atom (marked in blue) and removing a Si atom (marked beige) below the N atom. (b) A TED is inserted into the pristine crystal by displacing atoms according to the ES solution of TED (see Appendix B). The dislocation core is placed near the center of the simulation box between two *kk* planes (see Fig. 5). (c) The dislocation core is relaxed using the DFT calculation.

The lattice constants ($a = 3.091$ Å and $c = 10.129$ Å), and simulation parameters (cutoff energy $E_{\mathrm{cut}} = 350$ eV and k-mesh $2 \times 2 \times 1$) are determined by minimizing the total energy of one unit-cell. Lattice constants are found to be consistent with other findings in the literature [84]. Due to computational power concerns with a large number of atoms, we chose the k-mesh to be $2 \times 2 \times 1$.

Simulation box edges are chosen as $\langle a_1\rangle = 1/3\langle 2\bar{1}\bar{1}0\rangle$, $\langle a_2\rangle = 1/3\langle\bar{1}2\bar{1}0\rangle$, and $\langle c\rangle = \langle 0001\rangle$. To insert an edge dislocation within the crystal, we first construct a pristine crystal with edge lengths $7\langle a_1\rangle \times 7\langle a_2\rangle \times 1\langle c\rangle$ and insert an NV center in the *hh* configuration. The simulation box contains 391 atoms. We add a vacuum region surrounding the crystal with thickness $2\langle a_1\rangle$ to simulate an isolated TED within the DFT framework. The pristine crystal is shown in Fig. 6(a). Note that in this projection (zone axis $\langle 0001\rangle$), the Si vacancy is behind the N atom. The crystal is surrounded with a vacuum region in the directions normal to the dislocation line to simulate an isolated TED in a fully periodic simulation box. We insert a TED near the center of the box between two *kk* planes (see Fig. 5) by displacing the atoms using the ES solution for TED. The details of the ES calculation are discussed in Appendix B. The structure after the insertion of the TED is shown in Fig. 6(b). Subsequently, the TED-NV structure is relaxed using vasp with the simulation parameters discussed in step 1. The final atomic configuration [see Fig. 6(c)] exhibits a dislocation core structure that is similar to the previous study in the literature where a dipole of TEDs is simulated in a fully periodic simulation cell [85]. Hence, the effect of free surfaces near the dislocation core is minimal for our demonstration purposes. Note that the resulting TED core structure is similar to other first-principles calculations of TEDs in the literature [85]. The red atoms are excluded from consideration for RGFMD calculations since they exhibit spurious atomic displacements due to free surface effects.

The RGFMD framework requires the knowledge of atomic displacements to calculate the elastic displacement at every point within the crystal. However, the free surfaces cause the atoms to move spuriously. To minimize the effect of the free surfaces on the RGFMD calculations, we exclude the atoms directly on the free surface [marked with red in Fig. 6(c)].

D. Results

In this section, we demonstrate an application of the RGFMD framework. Our chosen model system is a TED within the 4H-SiC crystal. TEDs have dislocation lines along the $\langle c\rangle$ axis and Burgers vectors along the $\langle a\rangle$ direction of the hexagonal lattice. To fully demonstrate the utility of the RGFMD framework in investigating the elastic interactions between different lattice defects, we also insert an NV center near the dislocation core. NV centers' functional properties (such as spin coherence times) are also shown to be sensitive to the applied strain on the lattice. Hence, we believe our results will be valuable for accurate modeling and tuning of these functional point defects. The details of the *ab initio* simulations that are prerequisite for RGFMD calculations are discussed in Sec II C. The force density fields that represent the individual atoms within the system are calculated by assuming GGA for exchange-correlation effects as discussed in Sec. II B. Figures 7(a) and 7(b) illustrate the relaxed structure of the lattice with a TED and an NV center projected through $\langle 0001\rangle$ and $\langle 2\bar{1}\bar{1}0\rangle$, respectively. Note that the predicted dislocation core structure is similar to the other studies on TEDs [85].

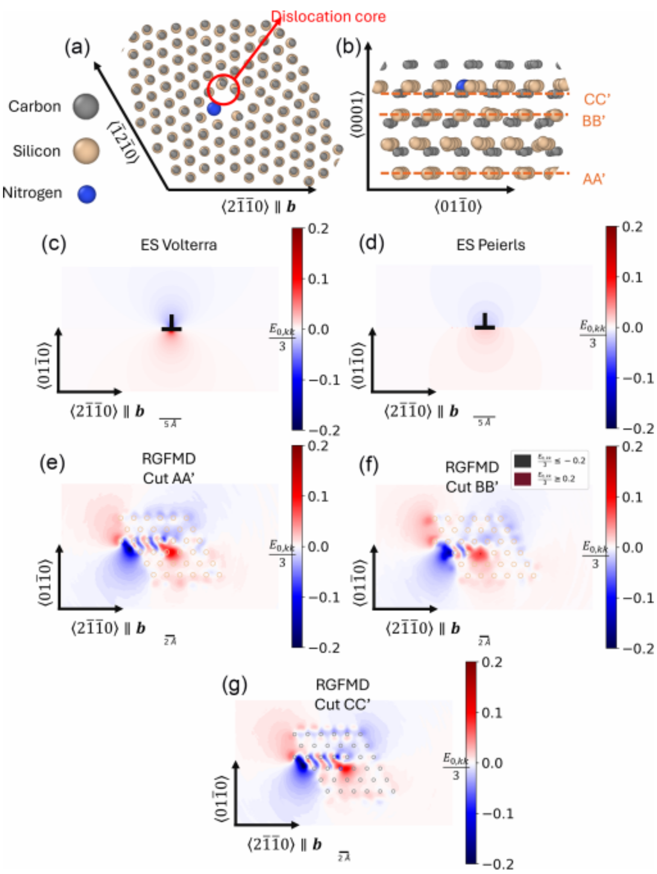

FIG. 7. Threading edge dislocation. (a) Relaxed structure of dislocation core and NV center projected through $\langle 0001\rangle$. (b) Relaxed structure of dislocation core and NV center projected through $\langle 2\bar{1}\bar{1}0\rangle$. (c) Strain field of an anisotropic Volterra dislocation calculated by ES framework. Note that Volterra dislocations generate a singularity at the dislocation core. (d) Strain field of an anisotropic Peierls-Nabarro (PN) dislocations. PN dislocation model removes the singularity at the dislocation core by representing the dislocation as a distribution of infinitesimal dislocations. (e)–(g) The strain field calculated by RGFMD projected onto cut planes *AA*', *BB*', and *CC*', respectively.

Dislocations generate large displacements and strains near their core. Hence, it is necessary to adopt an appropriate large strain measure. Due to its intuitiveness, we adopt logarithmic (also known as Hencky, or true strain) strain, $\boldsymbol{E}_0$, in our plots [86]. For a given deformation gradient tensor $\boldsymbol{F}$, the logarithmic strain $\boldsymbol{E}_0$ can be calculated as follows:

$$\boldsymbol{E}_0 = \tfrac{1}{2}\ln \boldsymbol{C},$$
$$\boldsymbol{C} = \boldsymbol{F}^T\boldsymbol{F}, \tag{15}$$

where $\boldsymbol{F}^T$ is the transpose of $\boldsymbol{F}$. Following Eq. (15), the volumetric part of the logarithmic strain becomes $\boldsymbol{E}_0^V = \frac{1}{3}\boldsymbol{E}_{0,kk}\boldsymbol{I}$, where $\boldsymbol{I}$ is the second-order identity tensor and $\boldsymbol{E}_{0,kk}$ is the trace of $\boldsymbol{E}_0$. To compare RGFMD with the conventional dislocation model, we calculate the strain field of an anisotropic Volterra dislocation with ES formalism, as discussed in Appendix B. The volumetric strain field of a Volterra dislocation is shown in Fig. 7(c). Volterra dislocations generate strain fields that exhibit a singularity at the center [39]. Hence, we exclude the core region of the strain field where strains tend to infinity in Fig. 7(c). We provide further comparisons in Appendix D for both the core domains and for far fields where the results converge.

Since the singular solutions for the elastic fields are unphysical at the core, one conventional method to model dislocation cores is to utilize the PN dislocation model [87]. The PN framework models dislocation cores as a distribution of infinitesimal dislocations known as dislocation density ρ. A common choice for dislocation density is the Lorentz distribution [87,88]

$$\rho(x) = \frac{b}{\pi}\frac{\xi}{x^2 + \xi^2}, \tag{16}$$

where x is the position measured along the Burgers vector of the dislocation, b is the magnitude of the Burgers vector, and ξ is the dislocation core width. Using the density of dislocations at a given point on the slip plane, the total strain at a point can be calculated by integrating the contribution of all the infinitesimal dislocations as follows:

$$^{\mathrm{ES,\ total}}(x, y) = \int_{-} \rho(t)\ ^{\mathrm{ES}}(x - t, y)dt, \tag{17}$$

where $^{\mathrm{ES}}(x, y)$ is the strain at point (x, y) as calculated by ES formalism as discussed in Appendix B. For our calculations, we chose the dislocation core width to be $\xi = 2.5$ Å, without loss of generality. The resulting PN dislocation strain field is plotted in Fig. 7(d). Contrary to Volterra dislocation, PN dislocations do not generate singularities at the core. However, both PN and Volterra models implicitly assume plane strain conditions. Hence, the resulting strain field do not vary along the dislocation line even though the local atomic configuration varies along the dislocation line. RGFMD addresses this problem since it does not assume plane strain conditions as discussed in Sec. II A.

While conventional continuum models of dislocations clearly denote a compressive and a tensile region above and below the slip plane, RGFMD predicts a strong angular dependence of tensile and compressive regions of the elastic strains. Moreover, the elastic fields predicted by RGFMD are functions of the local atomic displacements even at the core of the dislocation while ES formalism is not informed by the local atomic configuration. Figures 7(f) and 7(g) show the combined volumetric strain field of the TED core and Si vacancy and N substitutional atom of the NV center, respectively. Figures 7(e)–7(g) show the volumetric strain field at different cuts of the relaxed structure. Cuts *AA*', *BB*', and *CC*' [Figs. 7(e)–7(g)] are all projected through the $\langle 0001\rangle$ axis as examples of different planes far or close to the discloation core. A comparison of the three methods is also provided in Fig. 12 in Appendix D with strain versus radial distance plots. By comparing Figs. 7(e)–7(g) it can be said that the Si vacancy creates a tensile strain field and N atom creates a compressive strain field. Conventionally, point defects are assumed to create uniform lattice distortions. However, these conventional assumptions are not sufficient to predict the elastic fields of point defects accurately. Along the dislocation line, planes of Si and C atoms are stacked on top of each other to form the 4H-SiC crystal. The difference in the atomic configuration and electronic structure of planes of different atomic species causes the predicted strain field to vary. Such variations cannot be predicted via ES formalism due to its implicit assumption of plane strain conditions. The variations of strain field conform to the periodicity of the lattice along the dislocation line. The lattice and the strain field are periodic along the ⟨0001⟩ axis, which is also chosen as the periodic boundary in DFT calculations. The RGFMD accurately captures the variation of the strain field along the dislocation line which has been omitted in classical elasticity solutions. Figures 7(f) and 7(g) show the strain field projected onto the planes containing Si vacancy and N substitutional atom, respectively.

III. DISCUSSION

RGFMD calculates continuum elastic fields of dislocations by bridging the gap between atomistics methodologies, where the dislocation core represented by discrete atoms and their interactions, and classical continuum elastic solutions of dislocations, where the continuous displacement field of a dislocation is computed by solving the force equilibrium equation. RGFMD leverages the fundamental information revealed by first-principles calculations such as atomic displacements and electron wave functions to calculate continuum elastic fields of dislocations. Within RGFMD, every atom is represented by a characteristic force density field that is calculated by using the electron wave functions and its gradient (see Sec. II B). Subsequently, RGFMD solves the force equilibrium equation by accounting the quasiperiodic nature of the dislocations (see Sec. II A). The resulting elastic fields are guaranteed to conform to the known nuclear displacements of the atoms; hence to accurately represent the atomic configuration of the dislocation core. Moreover, RGFMD can describe the variations in the elastic strain along the dislocation line as well (see Fig. 7), which cannot be revealed using classical elasticity solutions as discussed below.

Classical elasticity solutions of dislocations aim to solve the force equilibrium equation for prescribed displacement boundary conditions. Such displacement boundary conditions are usually parametrized via disregistry functions, which measure the relative displacements of atoms immediately below and above the slip plane with respect to each other, as proposed by Peierls [88]. Continuum elastic solutions generate diverging solutions at the core of the dislocation. Theivergent nature of the classical elasticity solutions prevents a complete description of dislocation elastic fields everywhere in a lattice. One attempt to resolve this shortcoming is to adopt the PN model. The PN model assumes that the disregistry function takes a smooth form, usually represented by the arctan function from which the relative nuclear displacements of atoms above and below the slip plane can be sampled. This method eliminates the singularity at the core [see Fig. 8(a)]. However, the PN model for dislocations relies on the assumption of plane strain conditions. Consequently, it is not possible to capture the variations of elastic displacements along the dislocation line as shown in Figs. 8(b) and 8(c). Moreover, local atomic displacements near the core may not always conform to monotonically increasing disregistry functions. RGFMD addresses these challenges by enforcing the atomic displacements (which are calculated through DFT calculations) as boundary conditions and representing individual atoms with regularized Green's functions [see Fig. 8(d)]. Consequently, RGFMD is capable of calculating the variation of elastic fields in three dimensions without singularities even in the presence of point defects. Figure 8(d) illustrates the cross section of the displacement field calculated by the RGFMD framework. To compare the RGFMD displacement fields against PN displacement fields, the displacement fields are plotted on the cross sections immediately above and below the slip plane as well [see Figs. 8(b), 8(c), 8(e), and 8(f)]. Clearly, the local atomic configuration around the slip plane creates nontrivial variations in the displacement field. For example, in the case of TED in the 4H-SiC case, two *kk* planes (see Fig. 5) immediately above and below the slip plane of TED are not exactly symmetric but are translated with respect to each other. Hence, the resulting displacement fields are neither monotonous along the Burger vector direction $\langle 2\bar{1}\bar{1}0\rangle$ nor constant along the dislocation line direction ⟨0001⟩ [see Figs. 8(e) and 8(f)]. This effect cannot be captured via classical elasticity solutions for dislocations [see Figs. 8(b) and 8(c)]. Indeed, the PN formulation has been founded on the assumption of simple cubic crystals where all planes above and below the slip plane are symmetric. Hence, we believe RGFMD is a critical tool for bridging the gap between atomistic and continuum models of dislocations.

In summary, as discussed in Sec. II C, a TED is inserted between two *kk* planes (see Fig. 5). Even though these *kk* planes have the same atomic density, atomic sites within them are translated with respect to each other. Consequently, the displacement field on these planes is not monotonously changing along the Burgers vector direction $\langle 2\bar{1}\bar{1}0\rangle$, and is not constant along the dislocation line ⟨0001⟩. The three-dimensional nature of the elastic fields [Figs. 8(d)–8(f)] of dislocations is not captured with PN calculations [Fig. 8(a)–8(c)].

Atomistic methodologies, such as molecular dynamics (MD) and DFT, model dislocations as line defects within pristine lattices with periodic boundaries. The first-principles calculations model atoms as point-like entities and only account for the positional degrees of freedom of the atoms' nuclei. This simplification is necessary for the development of tractable solutions for the problems at hand from the atomistic point of view. However, as a result, the displacement field can only be calculated as a discrete field defined at lattice sites. Such a discrete description of the elastic fields does not conform with the well-established continuum elasticity where elastic quantities such as strain and displacement are given as fields. Moreover, atomistic methods calculate the total energy values of a given configuration by accounting for all interactions, including elastic interaction and interactions between defects and the boundaries. However, it is not always possible to decouple the elastic interactions from the total energy calculations. RGFMD provides an accurate method for mapping the discrete results of displacements calculated by *ab initio* methods onto a continuum field. Subsequently, the continuum fields predicted by RGFMD can be used to isolate elastic interactions.

In Fig. 4, we observe that the QMFD field is localized around atomic sites. The localization of QMFD field suggests the interatomic interactions to be dominated by short-range interactions. Our formulation for QMFD is derived from first principles and does not implicitly assume short-range

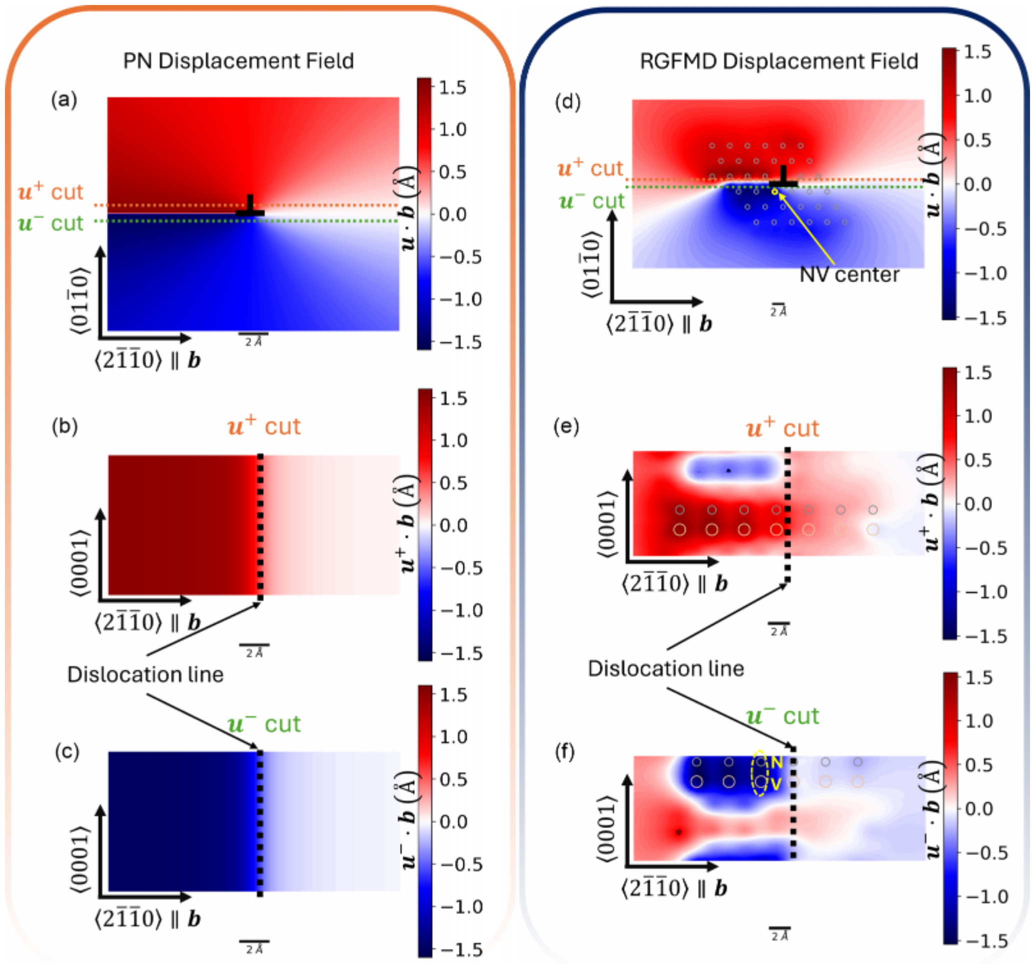

FIG. 8. TED displacement fields as calculated by the PN model and RGFMD. (a) The displacement field projected onto the plane normal to dislocation line direction ⟨0001⟩. Within the PN framework, the dislocation core is characterized by the relative displacement of atoms immediately (b) above ($\boldsymbol{u}^+$ cut) and (c) below the slip plane ($\boldsymbol{u}^-$ cut). Note that PN model does not account for the variations of the elastic fields along the dislocation line. (d) The cross-section (normal to ⟨0001⟩ direction) of the displacement field of a TED and NV center as predicted by RGFMD. This cross-section includes the N atom of NV center. Note that NV center does not lay on the slip plane of the inserted TED. The location of atoms are marked by tan (Si), gray (C), and blue (N) circles. RGFMD displacement field (e) above $\boldsymbol{u}^+$ cut and (f) below $\boldsymbol{u}^-$ cut.

interactions. Both the long- and short-range interactions between atoms are encoded within the electronic structure of the system when the DFT simulations are conducted under appropriate conditions. Hence, we would expect the long-range interactions such as van der Waals and ionic interactions to appear in the QMFD calculations. Indeed, the effect of surfaces and edges, where more complicated interactions than nearest-neighbor interactions appear, on the QMSD and QMFD has been successfully computed in [89]. The underlying framework of regularized Green's functions would still apply in these systems. However, for systems, where the long-range interactions are dictating the underlying physics, the behavior of QMFD would differ from what has been shown in this paper. We expect QMFD field to be *not* localized around atomic sites and *not* spherically symmetric when these long-range interactions are dominant. Under these conditions, the forcing function would be nonspherical $f(\boldsymbol{x}) \neq f(|\boldsymbol{x}|)$ [the transition from Eqs. (5) and (6) would not apply]. Depending on the form of the forcing function in $f(\boldsymbol{x})$, another convenient mathematical decomposition [similar to Eq. (6)] may be found.

We believe the implications of the RGFMD are far-reaching. For example, the PN model assumes the atomic motions to be in accordance with the Cauchy-Born hypothesis where atoms are expected be displaced according to the predictions of continuum elastic solutions. This consideration is an improvement over the Volterra dislocation model and has been extremely useful to describe the critical stress for a wide range of materials [4,9,10]. On the other hand, we have shown the divergence of the RGFMD and PN predictions near the dislocation cores in Fig. 7 of the original paper which is further elaborated on in Appendix D. The PN model predicts the strain field to be compressive on one side and tensile on the other. On the other hand, RGFMD predicts a much more complicated strain field that i varying along the dislocation line [Figs. 1(c) and 7]. Moreover, we have also made the comparison in terms of the displacement and disregistry fields near the dislocation core. In this aspect, the PN model has two drawbacks: it assumes a one-dimensional disregistry function that does not vary along the dislocation line and it is devised for simple cubic crystals. It is also important to note that waviness of a given dislocation can be observed from how the disregistry function varies along the dislocation line. In simple cubic lattices, atomic positions at above and below the slip plane coincide when projected through the slip normal. However, for TEDs, this is not the case (and will not be the case for most lattices) as shown in Figs. 5 and 8. Hence, the disregistry functions predicted by RGFMD takes a more complicated form as shown in Fig. 8. This result suggests that dislocations will inherently assume a wavy form within the crystal. These types of short-range interactions have long been shown to dictate the CRSS (Critical Resolved Shear Stress) the of dislocations [90–93].

One potential avenue of improvement for RGFMD is to incorporate the variability of the elastic properties of the material. Dislocation cores generate large strains in the short-range regime where the elastic properties of the underlying material may change [94–98]. In the case of varying elastic moduli, Eq. (1) needs to be converted into a more general form so that the elastic tensor C_{ijkl} is also a function of the position. The variation of the elastic moduli can be represented via a special blending function. Subsequently, the Green's function for the inhomogeneous system can be determined via a similar method given in Sec. II A. Alternatively, a statistical method such as walk-on-spheres [99,100] may be adopted to solve the Green's function for inhomogeneous materials. Recent developments on varying moduli fields have been shown in [101].

IV. CONCLUSIONS

In conclusion, this work proposes an analytical framework, RGFMD, to calculate the lattice distortions near the dislocation cores using the fundamental information obtained from DFT calculations. RGFMD models every atom within the lattice with a characteristic force distribution called QMFD. QMFD is related to electron wave functions, which are fundamental quantities reported by *ab initio* calculation codes. Subsequently, the force equilibrium equation is solved via Fourier transform in a computationally efficient manner. RGFMD incorporates the quasiperiodic nature of the dislocation core structure by accounting for the images of individual atoms along the dislocation line. Our work supports the following novel advancements over the conventional atomistic and classical elasticity methods for dislocations.

The classical elasticity force equilibrium equation for a prescribed displacement boundary condition representing the dislocation in elastic media. For anisotropic materials, this method is also known as the ES framework. The ES framework creates singularity at the core of the dislocation due to the implication of the applied point load along the dislocation line. The resulting divergent strain field precludes an accurate elastic description of the dislocation core with classical elasticity methods. Hence, conventionally, the core region is excluded from elastic field calculations. RGFMD circumvents this problem by introducing the bounded and well-defined QMFD fields representing the individual atoms near the dislocation core. The resulting elastic fields are guaranteed to be bounded and finite.

The ES framework is built upon the assumption of plane strain conditions. Consequently, the elastic fields calculated via the ES framework vary only within the plane that is normal to the slip. However, the atomic configuration and the elastic behavior vary along the dislocation line. Naturally, the elastic fields of the dislocations must conform to the periodicity of the underlying lattice in the threading direction of the dislocation. This behavior is completely missed in classical elasticity solutions. RGFMD accurately captures the variations in the elastic fields along the dislocation line since it takes the nuclear displacements of the atoms in three dimensions as boundary conditions.

First-principles calculations of line defects determine the nuclear positions of atoms near the dislocation core via minimization of the total energy of the system. To produce tractable solution schemes, atomistic methodologies reduce the degree of freedom of every atom to its nucleus' positional degree of freedom. This simplification bestows a discrete nature upon the results of atomistic calculations. Consequently, it is not possible to derive *field* representations of elastic variables such as displacement and strain directly from *ab initio* calculations. RGFMD bridges this gap between *ab initio* calculations and continuum field theories. RGFMD takes the discrete atomic displacement and QMFD data obtained via first-principles calculations and generates the continuum elastic fields of a dislocation core. By its derivation, the results of the RGFMD calculation are guaranteed to fit the known atomic displacements calculated using the *ab initio* methods.

Ab initio calculations necessitate the use of periodic or free surface boundary conditions. First-principles codes calculate and minimize the total energy of the given system, which includes the elastic energy of the point and line defects contained within, as well as interactions between the defects and the boundary conditions. However, it is not easy to decouple these contributions to isolate the elastic interactions of the point and line defects that are under investigation. By solving the force equilibrium equation for infinite media, RGFMD provides an efficient way to decouple the elastic interaction from the boundary conditions that are imposed by the simulation. The elastic interactions between point and line defects are known to affect the functional and mechanical properties of materials. One example of such a phenomenon is the interaction between NV centers and TEDs in 4H-SiC. As a promising qubit, NV centers' spin properties are shown to be affected by elastic distortions on the lattice. Hence, this study also aims to provide insight into the possibility of utilizing TEDs to tune the spin properties of NV centers for quantum computing applications.

ACKNOWLEDGMENTS

This paper is based upon work supported by the U.S. Airforce, Office of Scientific Research, under Award No. FA9550-22-1–0314, and partially by the National Science Foundation Grants No. NSF-DMR 2104971 and No. NSF-CMMI-21–25821. This work used the Illinois Campus Cluster, a computing resource operated by the Illinois Campus Cluster Program (ICCP) and the Delta research computing

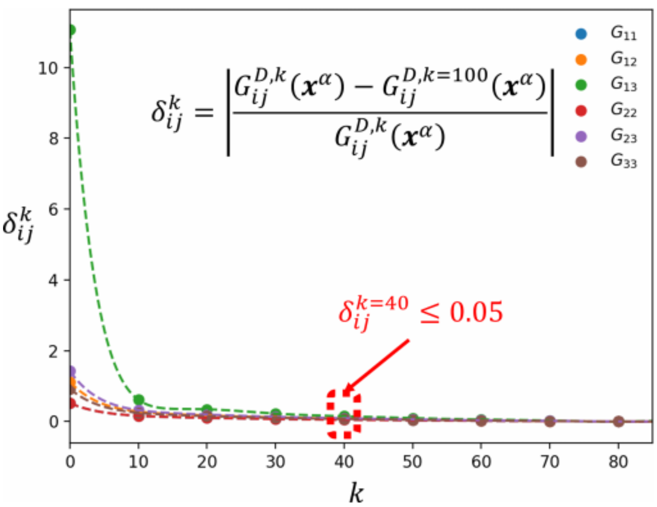

FIG. 9. The effect of truncation of periodic images on the precision of RGFMD calculation. See text for details.

project, which is supported by the National Science Foundation (Award No. OCI 2005572), and the State of Illinois. We also acknowledge the comment from the reviewer that led to the inclusion of additional figures in Appendixes C and D.

DATA AVAILABILITY

The data that support the findings of this article are not publicly available upon publication because it is not technically feasible and/or the cost of preparing, depositing, and hosting the data would be prohibitive within the terms of this research project. The data are available from the authors upon reasonable request.

APPENDIX A: CONVERGENCE OF RGFMD

Equations (6) and (8) can be used to compute the regularized Green's function due to a dislocation. Equation (8) simply sums up the infinitely many periodic images of the same Green's function along the dislocation line. Naturally, a practical implementation of RGFMD requires one to truncate the number of periodic images that are considered in the calculations. As the truncation limit increases the computational cost of calculating one dislocation Green's function increases linearly. In this study, we chose $k_{\max} = 40$ (i.e., 40 images of the regularized Green's function in both directions along the dislocation line are considered) as a compromise between computational efficiency and accuracy (Fig. 9). This choice has been made by evaluating the error introduced by the truncation in the individual components of the dislocation Green's function $\boldsymbol{G}^D$. We define the following error function:

$$\delta_{ij}^{k} = \left|\frac{G_{ij}^{D,k}(\boldsymbol{x}^{\alpha}) - G_{ij}^{D,k=100}(\boldsymbol{x}^{\alpha})}{G_{ij}^{D,k}(\boldsymbol{x}^{\alpha})}\right|. \tag{A1}$$

By this metric, the relative error in Green's function components G_{11}, G_{22}, and G_{33} calculated at the center of an atom are all lower than 0.05 when $k_{\max} = 40$. Hence, we propose $k_{\max} = 40$ as a reasonable compromise between computational cost and accuracy.

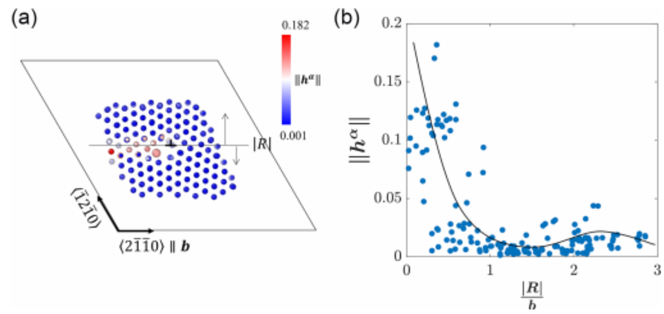

FIG. 10. Plot of scaling vector ($\boldsymbol{h}^{\alpha}$) magnitude along the absolute distance (R) from the slip; the distance is normalized by burgers vector magnitude.

APPENDIX B: ESHELBY-STROH FORMALISM FOR DISLOCATIONS IN ANISOTROPIC MEDIA

We briefly describe the ES formalism here for convenience. See [36–38] for a more detailed exposition. First, we define a coordinate with three vectors $\hat{\boldsymbol{m}}$, $\hat{\boldsymbol{n}}$, and $\hat{\boldsymbol{t}}$. The coordinate system is chosen so that $\hat{\boldsymbol{t}}$ is parallel to the dislocation line, $\hat{\boldsymbol{m}}$ is a vector within the slip plane and normal to the dislocation line, and $\hat{\boldsymbol{n}}$ is normal to the slip plane. The Eshelby-Stroh formalism solves the anisotropic force equilibrium equation of the following form:

$$C_{ijkl}\frac{\partial u_k}{\partial x_j \partial x_l} = 0. \tag{B1}$$

To solve Eq. (B1), we introduce the Eshelby-Stroh constants p_α and $A_{k\alpha}$. ES constants can be found by solving the following equations:

$$\begin{aligned} C_{ijkm}(m_i + p_\alpha n_i)(m_m + p_\alpha n_m)A_{k\alpha} &= 0,\\ \|C_{ijkm}(m_i + p_\alpha n_i)(m_m + p_\alpha n_m)\| &= 0,\\ -n_i C_{ijkm}(m_m + p_\alpha n_m)A_{k\alpha} &= L_{j\alpha}, \end{aligned} \tag{B2}$$

where $\alpha = 1, 2, 3, \ldots, 6$, $k = 1, 2, 3$ and the Einstein summation convention is followed. ES constants are, in general, complex valued. The components of ES constants are arranged following the convention as follows:

$$\begin{aligned} p_{\alpha+3} &= \bar{p}_\alpha,\\ A_{k\alpha+3} &= \bar{A}_{k\alpha}, \end{aligned} \tag{B3}$$

where $\alpha = 1, 2, 3$ and $\bar{x}$ is a complex conjugate of x. Subsequently, the displacement field for a dislocation can be calculated with the following formula:

$$\begin{aligned} u_i &= \frac{1}{2\pi i}\sum_{\alpha=1}^{6}\eta_\alpha A_{i\alpha}L_{s\alpha}b_s \ln{(m_k x_k + n_k x_k p_\alpha)},\\ \eta_\alpha &= \begin{array}{l} 1 \text{ for } \alpha \in \{1, 2, 3\},\\ -1 \text{ for } \alpha \in \{4, 5, 6\}, \end{array} \end{aligned} \tag{B4}$$

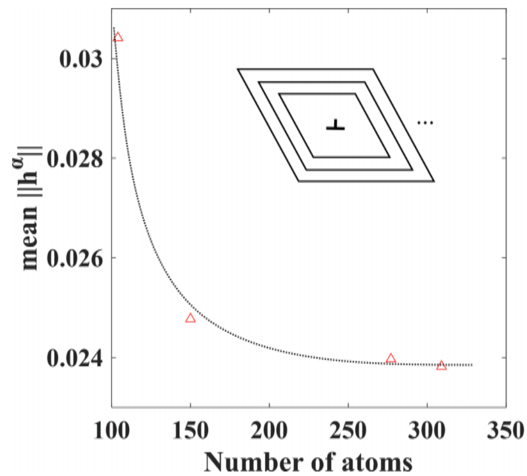

FIG. 11. Convergence of scaling vector ($\boldsymbol{h}^\alpha$) magnitude for each number of atoms with respect to field size.

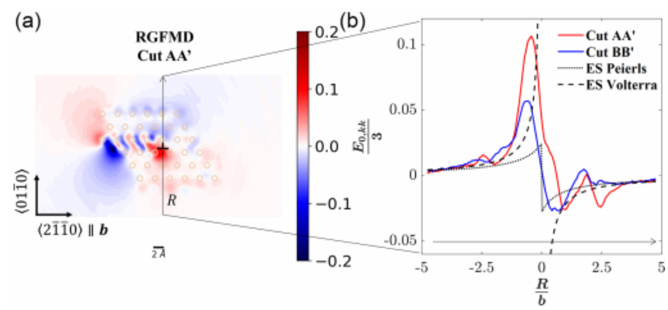

FIG. 12. Plot of $\frac{1}{3}\boldsymbol{E}_{0,kk}$ field of each classical (Stroh-based) and RGFMD on the same line profile including far away from the dislocation core. (a) The strain field calculated by RGFMD projected onto cut planes *AA*' with the notation of profile placing. (b) Line profiles of strain field of each model (ES Peierls, ES Volterra, and RGFMD). Two example cuts [*AA*' and *BB*' planes, depicted in Fig. 7(b)] from the RGFMD are shown; the line profile distance is normalized by burgers vector magnitude.

where $i^2 = -1$. Note that the displacement field $u_i(\boldsymbol{x})$ does not vary along the dislocation line $\hat{\boldsymbol{t}}$,

$$\boldsymbol{u}(\boldsymbol{x}) = \boldsymbol{u}(\boldsymbol{x} + a\hat{\boldsymbol{t}}), \quad \text{for } a \in \mathbb{R}. \tag{B5}$$

ES formalism starts its derivation by assuming the displacement field is a function of the position within the plane normal to the dislocation line leading to the invariance of the displacement field [see Eqs. (B4) and (B5) along the dislocation line]. Basically, it is a two-dimensional (2D) formulation. In our formalism, RGFMD, we do not resort to such a mathematical simplification. Instead, RGFMD solves the displacement field by directly solving the force equilibrium equation in three dimensions and enforcing the known atomic (nuclei) displacements as boundary conditions.

APPENDIX C: SCALING VECTOR (h^α) DISTRIBUTION AND CONVERGENCE

The change of the scaling vector ($\boldsymbol{h}^\alpha$ parameters) as a function of distance from the dislocation core, as well as the field convergence with the number of $\boldsymbol{h}^\alpha$ parameters are shown for reference. In Fig. 10, the scaling vector magnitude is shown in terms of the Euclidean norm, with respect to the normalized distance from the slip. The scatter of data is driven from different corrugated planes such as (*hh* and *kk*) along the entire supercell after relaxation. In Fig. 11, the average of the scaling vector magnitude for the different number of atoms is plotted.

APPENDIX D: STRAIN FIIELD COMPARISON AWAY FROM THE DISLOCATION CORE

As an extension of Fig. 7, the strain fields are compared at and away from the dislocation core in Fig. 12. It is shown that fields align from the dislocation core for both ES models and RGFMD. At distances further away from the dislocation core, the classical models show a comparable level of strain field for normalized distances *R/b* larger than 2.5 [Fig. 12(b)]. However, near the core of the dislocation the Volterra solution gives unbounded strains while the Peierls solution provides much lower strains [Fig. 12(b)]. The RGFMD falls between these two extremes and provides bounded strains of the order of 0.1.

[1] D. You, O. K. Celebi, A. S. K. Mohammed, D. W. Abueidda, S. Koric, and H. Sehitoglu, CRSS determination combining *ab-initio* framework and surrogate neural networks, Int. J. Plast. **162**, 103524 (2023).
[2] A. D. Rollett and U. Kocks, A review of the stages of work hardening, Solid State Phenom **35**, 1 (1993).
[3] N. F. Mott, CXVII. A theory of work-hardening of metal crystals, Lond. Edinb. Dubl. Phil. Mag. **43**, 1151 (1952).
[4] A. S. K. Mohammed, O. K. Celebi, and H. Sehitoglu, Critical stress prediction upon accurate dislocation core description, Acta Mater. **233**, 117989 (2022).
[5] F. Lavrentev, The type of dislocation interaction as the factor determining work hardening, Mater. Sci. Eng. **46**, 191 (1980).
[6] J. Koehler, The nature of work-hardening, Phys. Rev. **86**, 52 (1952).
[7] U. Kocks, Laws for work-hardening and low-temperature creep, J. Eng. Mater. Technol. **98**, 76 (1976).
[8] U. Kocks, A statistical theory of flow stress and work-hardening, Philos. Mag. **13**, 541 (1966).
[9] O. K. Celebi, A. S. K. Mohammed, and H. Sehitoglu, Effect of dislocation character on the CRSS, Acta Mater. **254**, 118982 (2023).
[10] O. K. Celebi, A. S. K. Mohammed, J. A. Krogstad, and H. Sehitoglu, Evolving dislocation cores at twin boundaries: Theory of CRSS elevation, Int. J. Plast. **148**, 103141 (2022).
[11] O. K. Celebi, G. Gengor, D. You, A. S. K. Mohammed, A. Bucsek, and H. Sehitoglu, Distorted dislocation cores and asymmetric glide resistances in titanium, Acta Mater. **274**, 119967 (2024).

[12] B. G. Butler, J. D. Paramore, J. P. Ligda, C. Ren, Z. Z. Fang, S. C. Middlemas, and K. J. Hemker, Mechanisms of deformation and ductility in tungsten–A review, Int. J. Refract. Met. Hard Mater **75**, 248 (2018).
[13] K. Tanaka, and T. Mura, A dislocation model for fatigue crack initiation, J. Appl. Mech. **48**, 97 (1981).
[14] D. Kuhlmann-Wilsdorf and C. Laird, Dislocation behavior in fatigue, Mater. Sci. Eng. **27**, 137 (1977).
[15] V. Deshpande, A. Needleman, and E. Van der Giessen, Discrete dislocation modeling of fatigue crack propagation, Acta Mater. **50**, 831 (2002).
[16] V. Deshpande, A. Needleman, and E. Van der Giessen, A discrete dislocation analysis of near-threshold fatigue crack growth, Acta Mater. **49**, 3189 (2001).
[17] S. Alkan and H. Sehitoglu, Nonuniqueness of the fatigue threshold, Int. J. Fatigue **104**, 309 (2017).
[18] Y. Bu, H. Yoshimoto, N. Watanabe, and A. Shima, Fabrication of 4H-SiC PiN diodes without bipolar degradation by improved device processes, J. Appl. Phys. **122**, 244504 (2017).
[19] M. Kato, O. Watanabe, T. Mii, H. Sakane, and S. Harada, Suppression of stacking-fault expansion in 4H-SiC PiN diodes using proton implantation to solve bipolar degradation, Sci. Rep. **12**, 18790 (2022).
[20] P. Pirouz and A. Galeckas, Degradation of SiC bipolar devices: A review of likely causes and recent advances in its understanding, ECS Trans. **41**, 225 (2011).
[21] H. Tsuchida, K. Murata, T. Tawara, M. Miyazato, T. Miyazawa, and K. Maeda, Suppression of bipolar degradation in 4H-SiC power devices by carrier lifetime control, in *2019 IEEE International Electron Devices Meeting (IEDM)*, (IEEE, New York, 2019), pp. 20.1. 1–20.1. 4.
[22] G. Love, Dislocation pipe diffusion, Acta Metall. **12**, 731 (1964).
[23] H. K. Birnbaum and P. Sofronis, Hydrogen-enhanced localized plasticity—a mechanism for hydrogen-related fracture, Mater. Sci. Eng.: A **176**, 191 (1994).
[24] P. Sofronis, The influence of mobility of dissolved hydrogen on the elastic response of a metal, J. Mech. Phys. Solids **43**, 1385 (1995).
[25] B. Beschoten, E. Johnston-Halperin, D. Young, M. Poggio, J. Grimaldi, S. Keller, S. DenBaars, U. Mishra, E. Hu, and D. Awschalom, Spin coherence and dephasing in GaN, Phys. Rev. B **63**, 121202(R) (2001).
[26] B. Liu, D. Raabe, P. Eisenlohr, F. Roters, A. Arsenlis, and G. Hommes, Dislocation interactions and low-angle grain boundary strengthening, Acta Mater. **59**, 7125 (2011).
[27] P. Pant, K. Schwarz, and S. P. Baker, Dislocation interactions in thin FCC metal films, Acta Mater. **51**, 3243 (2003).
[28] M. Zaiser, M.-C. Miguel, and I. Groma, Statistical dynamics of dislocation systems: The influence of dislocation-dislocation correlations, Phys. Rev. B **64**, 224102 (2001).
[29] R. Bullough and R. Newman, The kinetics of migration of point defects to dislocations, Rep. Prog. Phys. **33**, 101 (1970).
[30] J. F. Justo, M. de Koning, W. Cai, and V. V. Bulatov, Point defect interaction with dislocations in silicon, Mater. Sci. Eng.: A **309**, 129 (2001).
[31] A. Seeger, The kink picture of dislocation mobility and dislocation-point-defect interactions, Le Journal De Physique Colloques **42**, C5 (1981).
[32] I. Beyerlein, M. Demkowicz, A. Misra, and B. Uberuaga, Defect-interface interactions, Prog. Mater Sci. **74**, 125 (2015).
[33] S. Rao and P. Hazzledine, Atomistic simulations of dislocation–interface interactions in the Cu-Ni multilayer system, Philos. Mag. A **80**, 2011 (2000).
[34] J. Wang, R. Hoagland, J. Hirth, and A. Misra, Atomistic modeling of the interaction of glide dislocations with "weak" interfaces, Acta Mater. **56**, 5685 (2008).
[35] J. Wang, R. Hoagland, X. Liu, and A. Misra, The influence of interface shear strength on the glide dislocation–interface interactions, Acta Mater. **59**, 3164 (2011).
[36] A. Stroh, Dislocations and cracks in anisotropic elasticity, Philos. Mag. **3**, 625 (1958).
[37] A. Stroh, Steady state problems in anisotropic elasticity, J. Math. Phys. **41**, 77 (1962).
[38] T. C. Ting, *Anisotropic Elasticity: Theory and Applications* (Oxford University Press, New York, 1996).
[39] P. M. Anderson, J. P. Hirth, and J. Lothe, *Theory of Dislocations* (Cambridge University Press, Cambridge, England, 2017).
[40] J. Sinclair, P. Gehlen, R. Hoagland, and J. Hirth, Flexible boundary conditions and nonlinear geometric effects in atomic dislocation modeling, J. Appl. Phys. **49**, 3890 (1978).
[41] E. B. Tadmor, M. Ortiz, and R. Phillips, Quasicontinuum analysis of defects in solids, Philos. Mag. A **73**, 1529 (1996).
[42] G. Gengor, O. K. Celebi, A. S. K. Mohammed, and H. Sehitoglu, Continuum strain of point defects, J. Mech. Phys. Solids **188**, 105653 (2024).
[43] J. L. Ericksen, On the Cauchy-Born rule, Math. Mech. Solids **13**, 199 (2008).
[44] M. Pitteri and G. Zanzotto, *Continuum Models for Phase Transitions and Twinning in Crystals* (Chapman & Hall/CRC, Boca Raton, FL, 2003).
[45] Y. Zhu, B. Kovos, M. Onizhuk, D. Awschalom, and G. Galli, Theoretical and experimental study of the nitrogen-vacancy center in 4H-SiC, Phys. Rev. Mater. **5**, 074602 (2021).
[46] H. J. von Bardeleben, J. L. Cantin, A. Csóré, A. Gali, E. Rauls, and U. Gerstmann, NV centers in 3 C, 4 H, and 6 H silicon carbide: A variable platform for solid-state qubits and nanosensors, Phys. Rev. B **94**, 121202(R) (2016).
[47] D. D. Awschalom, R. Hanson, J. Wrachtrup, and B. B. Zhou, Quantum technologies with optically interfaced solid-state spins, Nat. Photon. **12**, 516 (2018).
[48] A. Csóré, H. Von Bardeleben, J.-L. Cantin, and A. Gali, Characterization and formation of NV centers in 3*C*, 4*H*, and 6*H* SiC: An *ab initio* study, Phys. Rev. B **96**, 085204 (2017).
[49] E. Herbschleb, H. Kato, Y. Maruyama, T. Danjo, T. Makino, S. Yamasaki, I. Ohki, K. Hayashi, H. Morishita, and M. Fujiwara, Ultra-long coherence times amongst room-temperature solid-state spins, Nat. Commun. **10**, 3766 (2019).
[50] J. Teissier, A. Barfuss, P. Appel, E. Neu, and P. Maletinsky, Strain coupling of a nitrogen-vacancy center spin to a diamond mechanical oscillator, Phys. Rev. Lett. **113**, 020503 (2014).
[51] F. La Via, M. Camarda, and A. La Magna, Mechanisms of growth and defect properties of epitaxial SiC, Appl. Phys. Rev. **1**, 031301 (2014).
[52] H. Matsunami and T. Kimoto, Step-controlled epitaxial growth of SiC: High quality homoepitaxy, Mater. Sci. Eng. R: Rep. **20**, 125 (1997).

[53] T. Kimoto, Material science and device physics in SiC technology for high-voltage power devices, Jpn J Appl Phys **54**, 040103 (2015).

[54] J. J. Li, G. Yang, X. S. Liu, H. Luo, L. B. Xu, Y. Q. Zhang, C. Cui, X. D. Pi, D. R. Yang, and R. Wang, Dislocations in 4H silicon carbide, J. Phys. D Appl. Phys. **55**, 463001 (2022).

[55] P. Fiorenza, M. S. Alessandrino, B. Carbone, C. Di Martino, A. Russo, M. Saggio, C. Venuto, E. Zanetti, F. Giannazzo, and F. Roccaforte, Understanding the role of threading dislocations on 4H-SiC MOSFET breakdown under high temperature reverse bias stress, Nanotechnology **31**, 125203 (2020).

[56] Y. A. Mitropolsky, A. M. Samoilenko, and D. I. Martinyuk, *Systems of Evolution Equations with Periodic and Quasiperiodic Coefficients*, 1st ed. (Kluwer, Dordrecht, The Netherlands, 1993).

[57] P. A. M. Dirac, *The Principles of Quantum Mechanics* (Oxford University Press, New York, 1981).

[58] L. D. Landau, E. M. Lifshitz, A. M. Kosevich, and L. P. Pitaevski, *Theory of Elasticity* (Elsevier, Amsterdam, 1986), Vol. 7.

[59] O. Nielsen and R. M. Martin, Quantum-mechanical theory of stress and force, Phys. Rev. B **32**, 3780 (1985).

[60] W. Pauli, *General Principles of Quantum Mechanics* (Springer Science & Business Media, New York, 2012).

[61] R. G. Newton, *Scattering Theory of Waves and Particles* (Springer Science & Business Media, New York, 2013).

[62] J. Chen and M. Desbrun, Go green: General regularized Greens functions for elasticity, in *ACM SIGGRAPH 2022 Conference Proceedings* (ACM, New York, 2022), pp. 1–8.

[63] P. C. Martin and J. Schwinger, Theory of many-particle systems. I, Phys. Rev. **115**, 1342 (1959).

[64] O. Nielsen and R. M. Martin, First-principles calculation of stress, Phys. Rev. Lett. **50**, 697 (1983).

[65] O. H. Nielsen and R. M. Martin, Stresses in semiconductors: *Ab initio* calculations on Si, Ge, and GaAs, Phys. Rev. B **32**, 3792 (1985).

[66] C. L. Rogers and A. M. Rappe, Geometric formulation of quantum stress fields, Phys. Rev. B **65**, 224117 (2002).

[67] Y. Shiihara, M. Kohyama, and S. Ishibashi, *Ab initio* local stress and its application to Al (111) surfaces, Phys. Rev. B **81**, 075441 (2010).

[68] S. Lehtola, C. Steigemann, M. J. Oliveira, and M. A. Marques, Recent developments in LIBXC—A comprehensive library of functionals for density functional theory, SoftwareX **7**, 1 (2018).

[69] W. Greiner, *Classical Electrodynamics* (Springer Science & Business Media, New York, 2012).

[70] J. D. Eshelby, The determination of the elastic field of an ellipsoidal inclusion, and related problems, Proc. R. Soc. Lond. Ser. A **241**, 376 (1957).

[71] J. D. Eshelby, The elastic field outside an ellipsoidal inclusion, Proc. R. Soc. Lond. Ser. A **252**, 561 (1959).

[72] I. Belabbas, J. Chen, M. I. Heggie, C. D. Latham, M. J. Rayson, P. R. Briddon, and G. Nouet, Core properties and mobility of the basal screw dislocation in wurtzite GaN: A density functional theory study, Modell. Simul. Mater. Sci. Eng. **24**, 075001 (2016).

[73] S. L. Frederiksen and K. W. Jacobsen, Density functional theory studies of screw dislocation core structures in bcc metals, Philos. Mag. **83**, 365 (2003).

[74] M. Ghazisaeidi and D. R. Trinkle, Core structure of a screw dislocation in Ti from density functional theory and classical potentials, Acta Mater. **60**, 1287 (2012).

[75] L. J. Wirth, A. A. Farajian, and C. Woodward, Density functional study of self-diffusion along an isolated screw dislocation in fcc Ni, Phys. Rev. Mater. **3**, 033605 (2019).

[76] S. K. Yadav, R. Ramprasad, A. Misra, and X. Y. Liu, Core structure and Peierls stress of edge and screw dislocations in TiN: A density functional theory study, Acta Mater. **74**, 268 (2014).

[77] S. Yin, J. Ding, M. Asta, and R. O. Ritchie, *Ab initio* modeling of the energy landscape for screw dislocations in body-centered cubic high-entropy alloys, npj Comput. Mater. **6**, 110 (2020).

[78] P. Pirouz, M. Zhang, J. L. Demenet, and H. M. Hobgood, Yield and fracture properties of the wide band-gap semiconductor 4H-SiC, J. Appl. Phys. **93**, 3279 (2003).

[79] T. Yahagi, T. Ohji, H. Yamaguchi, T. Takahashi, H. Nakano, M. Iijima, and J. Tatami, Deformation behavior and fracture strength of single-crystal 4H-SiC determined by microcantilever bending tests, Adv. Eng. Mater. **26**, 2400095 (2024).

[80] G. Kresse and J. Furthmüller, Efficient iterative schemes for *ab initio* total-energy calculations using a plane-wave basis set, Phys. Rev. B **54**, 11169 (1996).

[81] P. E. Blöchl, Projector augmented-wave method, Phys. Rev. B **50**, 17953 (1994).

[82] G. Kresse and D. Joubert, From ultrasoft pseudopotentials to the projector augmented-wave method, Phys. Rev. B **59**, 1758 (1999).

[83] J. P. Perdew, K. Burke, and M. Ernzerhof, Generalized gradient approximation made simple, Phys. Rev. Lett. **77**, 3865 (1996).

[84] M. Stockmeier, R. Müller, S. Sakwe, P. Wellmann, and A. Magerl, On the lattice parameters of silicon carbide, J. Appl. Phys. **105**, 033511 (2009).

[85] J. Łażewski, P. Jochym, P. Piekarz, M. Sternik, K. Parlinski, J. Cholewiński, P. Dłużewski, and S. Krukowski, DFT modelling of the edge dislocation in 4H-SiC, J. Mater. Sci. **54**, 10737 (2019).

[86] M. Latorre and F. J. Montáns, On the interpretation of the logarithmic strain tensor in an arbitrary system of representation, Int. J. Solids Struct. **51**, 1507 (2014).

[87] R. Peierls, The size of a dislocation, Proc. Phys. Soc. **52**, 34 (1940).

[88] W. Feller, *An Introduction to Probability Theory and its Applications* (John Wiley & Sons, New York, 1991), Vol. 2.

[89] A. Filippetti and V. Fiorentini, Theory and applications of the stress density, Phys. Rev. B **61**, 8433 (2000).

[90] C. Varvenne, G. P. M. Leyson, M. Ghazisaeidi, and W. A. Curtin, Solute strengthening in random alloys, Acta Mater. **124**, 660 (2017).

[91] D. You, O. K. Celebi, A. S. K. Mohammed, A. Bucsek, and H. Sehitoglu, The derivation of CRSS in pure Ti and Ti-Al alloys, Int. J. Plast. **184**, 104187 (2025).

[92] D. You, O. K. Celebi, G. Gengor, A. S. K. Mohammed, W. Abuzaid, and H. Sehitoglu, Short-range ordering mechanics in FCC materials, Int. J. Plast. **174**, 103919 (2024).

[93] D. You, O. K. Celebi, D. W. Abueidda, G. Gengor, A. S. K. Mohammed, S. Koric, and H. Sehitoglu,

Inverse design of short-range order arrangement via neural network, Int. J. Solids Struct. **309**, 113175 (2025).

[94] F. Birch, The effect of pressure on the modulus of rigidity of several metals and glasses, J. Appl. Phys. **8**, 129 (1937).

[95] F. Birch, in *Elasticity (except compressibility)*, edited by F. B. Chairman, J. F. Schairer, H. C. Spicer, Handbook of Physical Constants (Geological Society of America, 1942).

[96] P. W. Bridgman, *The Effect of Pressure on the Rigidity of Several Metals, Papers 59–93*, (Harvard University Press, Cambridge, MA, 1964), pp. 2379–2390.

[97] V. V. Bulatov, O. Richmond, and M. V. Glazov, An atomistic dislocation mechanism of pressure-dependent plastic flow in aluminum, Acta Mater. **47**, 3507 (1999).

[98] W. A. Spitzig and O. Richmond, The effect of pressure on the flow stress of metals, Acta Metall. **32**, 457 (1984).

[99] B. Miller, R. Sawhney, K. Crane, and I. Gkioulekas, Differential walk on spheres, ACM Trans. Graph. **43**, 174 (2024).

[100] R. Sawhney, D. Seyb, W. Jarosz, and K. Crane, Grid-free Monte Carlo for PDEs with spatially varying coefficients, ACM Trans. Graph. **41**, 53 (2022).

[101] G. Gengor, O. K. Celebi, A. S. K. Mohammed, and H. Sehitoglu, Quantum Mechanical Moduli Field, Acta Mater. 289, 120922 (2024).